The Ising triangular-lattice antiferromagnet neodymium heptatantalate as a quantum spin liquid candidate

T. Arh [1,2], B. Sana [3], M. Pregelj [1], P. Khuntia [3,4,5], Z. Jagličić [6,7], M. D. Le [8], P. K. Biswas [8], P. Manuel [8], L. Mangin-Thro [9], A. Ozarowski [10] and A. Zorko [1,2] ✉

Disordered magnetic states known as spin liquids are of paramount importance in both fundamental and applied science. A classical state of this kind was predicted for the Ising antiferromagnetic triangular model, while additional non-commuting exchange terms were proposed to induce its quantum version—a quantum spin liquid. However, these predictions have not yet been confirmed experimentally. Here, we report evidence for such a state in the triangular-lattice antiferromagnet $NdTa_7O_{19}$. We determine its magnetic ground state, which is characterized by effective spin-1/2 degrees of freedom with Ising-like nearest-neighbour correlations and gives rise to spin excitations persisting down to the lowest accessible temperature of 40 mK. Our study demonstrates the key role of strong spin–orbit coupling in stabilizing spin liquids that result from magnetic anisotropy and highlights the large family of rare-earth (RE) heptatantalates $RETa_7O_{19}$ as a framework for realization of these states, which represent a promising platform for quantum applications.

Quantum materials that are characterized by emergent quantum phenomena leading to unconventional functionalities represent the mainstream in modern condensed matter research[1–3]. One such intriguing phenomenon is a quantum entangled but magnetically disordered state known as a quantum spin liquid (SL), which is a natural ground-state contender on geometrically frustrated spin lattices[4–6]. Contrary to more common spin glasses also lacking magnetic order, a SL does not feature static internal magnetic fields. Initially, a SL ground state was proposed for a triangular-lattice antiferromagnet (TAFM) with Heisenberg interactions, that is, isotropic nearest-neighbour exchange interactions[7], but theory later converged on a magnetically ordered ground state[8]. Nevertheless, deviations from this model, such as next-neighbour[9] and spatially anisotropic exchange interactions[10], or magnetic anisotropy[11,12] can still stabilize SLs. In fact, the most anisotropic, that is, the classical Ising TAFM model including only the out-of-plane component of the exchange interaction $\mathcal{J}_z$, was the first spin model predicted to possess a disordered, macroscopically degenerated ground state—a classical SL—by Wannier in 1950 (ref. [13]). An additional in-plane component $\mathcal{J}_{xy}$ introduces quantum fluctuations[14] that lift the degeneracy of the ground-state manifold and eventually select magnetic order[11]. However, close to the Ising limit a quantum SL can potentially be realized[15,16]. Neither the classically disordered Wannier state nor its disordered quantum successor characterized by quantum fluctuations has been confirmed experimentally, which thus remains one of the fundamental quests in the field.

Materials with strongly spin–orbit-entangled local magnetic moments represent a natural habitat for SL states borne out of magnetic anisotropy on frustrated spin lattices[17,18], as well as for various other intriguing many-body quantum phenomena[19]. The RE-based $YbMgGaO_4$ compound is the most intensively investigated TAFM example of this kind[20–22]. However, its SL-like ground state likely emerges from sizeable structural disorder[23,24], similar to that proposed for other well-studied TAFM materials lacking magnetic order[25,26], including organic charge-transfer salts[27,28] and 1T-TaS_2 (ref. [29]). As the origin of the apparent SL character in all these materials remains debatable, disorder-free TAFM candidates are highly desired, especially RE-based ones[30–32], where large magnetic anisotropy could warrant the existence of SL ground states. Here we report the realization of such a state in a newly discovered RE-based TAFM material $NdTa_7O_{19}$. Its crystal-electric-field (CEF) ground-state Kramers doublet is characterized by highly anisotropic exchange interactions between the effective spin-1/2 degrees of freedom, $\mathcal{J}_z = 0.90(2)$ K and $\mathcal{J}_{xy} = 0.16(2)$ K. In absence of structural disorder, these Ising-like interactions are likely the key for stabilizing its quantum-disordered ground state with dominant Ising correlations down to at least 40 mK.

The hexagonal crystal structure (space group $P\bar{6}c2$) of the neodymium heptatantalate $NdTa_7O_{19}$ has been known for some time, yet its physical properties have been so far investigated only regarding applications in laser technology and nonlinear optics[33,34]. Here we highlight the triangular symmetry of well-separated layers of magnetic Nd^{3+} ions in this material (Fig. 1a), representing a highly sought after setting for realization of the two-dimensional TAFM. We investigate its magnetism by performing various complementary experimental techniques on high-quality polycrystalline samples. The details on sample synthesis and crystal structure are given in the Methods.

[1]Jožef Stefan Institute, Ljubljana, Slovenia. [2]Faculty of Mathematics and Physics, University of Ljubljana, Ljubljana, Slovenia. [3]Department of Physics, Indian Institute of Technology Madras, Chennai, India. [4]Quantum Centre for Diamond and Emergent Materials, Indian Institute of Technology Madras, Chennai, India. [5]Functional Oxide Research Group, Indian Institute of Technology Madras, Chennai, India. [6]Faculty of Civil and Geodetic Engineering, University of Ljubljana, Ljubljana, Slovenia. [7]Institute of Mathematics, Physics and Mechanics, Ljubljana, Slovenia. [8]ISIS facility, Rutherford Appleton Laboratory, Didcot, UK. [9]Institut Laue-Langevin, Grenoble, France. [10]National High Magnetic Field Laboratory, Florida State University, Tallahassee, FL, USA. ✉e-mail: andrej.zorko@ijs.si
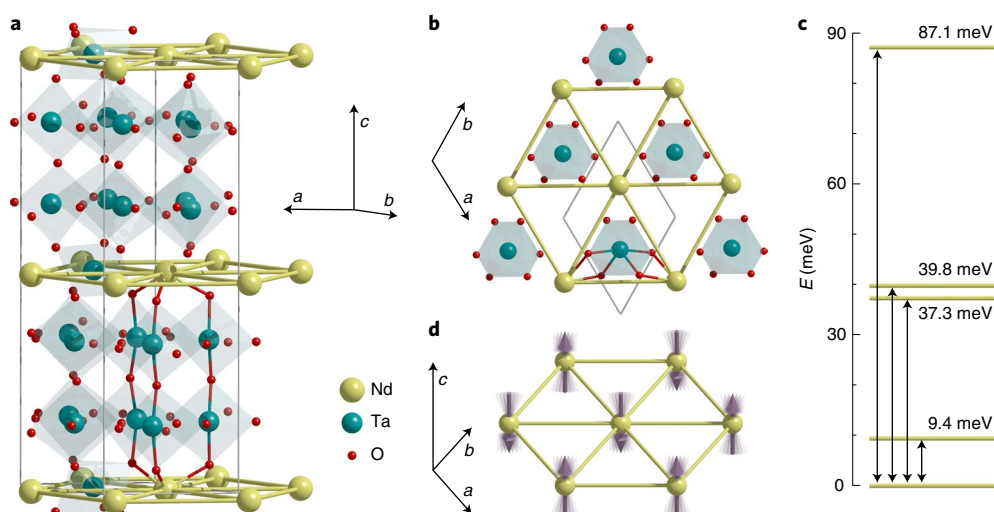
Fig. 1 | Crystal structure and magnetic ground state of NdTa$_7$O$_{19}$. a,b, In the hexagonal crystal structure of NdTa$_7$O$_{19}$ (space group $P\bar{6}c2$; thin grey lines show the unit cell) the two-dimensional triangular layers of magnetic Nd^{3+} ions ($^4I_{9/2}$) are well separated along the crystallographic c axis, making the interlayer –O–Ta–O–Ta–O– exchange bridges (represented by double-coloured bonds in **a** for two selected sites) much longer and therefore less effective than the intralayer bridges –O–Ta–O– (thin double-coloured bonds in **b**). **c,** The ground-state Kramers doublet is separated from other Kramers doublets of the $^4I_{9/2}$ multiplet due to CEF. **d,** Within the ground state, the corresponding $S=1/2$ effective spins (arrows) are dominantly antiferromagnetically coupled to nearest neighbours within layers (thick single-colour bonds), with the exchange interaction being characterized by strong Ising anisotropy along the crystallographic c axis, $\mathcal{J}_z = 0.90(2)$ K $\gg \mathcal{J}_{xy} = 0.16(2)$ K. This leads to a quantum SL ground state with no long-range magnetic order down to at least 40 mK and characteristic Ising-like correlations.

Bulk magnetic measurements (Methods) show no sign of magnetic ordering or freezing down to 1.9 K (Fig. 2), suggesting a possible dynamical magnetic ground state of NdTa$_7$O$_{19}$. At temperatures above 100 K, the inverse magnetic susceptibility $1/\chi$ follows the Curie–Weiss (CW) law (Fig. 2a; Methods) with the Weiss temperature $\theta_{CW}^h = -78(4)$ K and an effective magnetic moment $\mu_{eff}^h = 3.8(1)\mu_B$ of the Nd^{3+} ion, which is close to the free-ion value of $3.62\mu_B$, where μ_B is the Bohr magneton. The rather large value of θ_{CW}^h is not a sign of strong exchange interactions present in NdTa$_7$O$_{19}$. This is because the excited CEF levels of RE ions typically lie within a few millielectronvolts from the ground state and can strongly affect their magnetism, leading to situations with seemingly strong magnetic interactions even when these are in fact much weaker[35]. Indeed, after deviating from the high-temperature CW dependence below 100 K, a CW dependence is re-established below 4.2 K, but with drastically reduced $\theta_{CW}^l = -0.46(3)$ K and $\mu_{eff}^l = 1.9(1)\mu_B$ (Fig. 2b; Methods).

To understand the magnetism of NdTa$_7$O$_{19}$ and quantitatively assess its magnetic interactions, the knowledge of the Nd^{3+} CEF levels is first required. For this purpose the energy (E)- and wave-vector (**Q**)-dependent dynamical structure factor was measured at 5 K (Fig. 3) by inelastic neutron scattering (INS; Methods), which directly detects the CEF transitions. The INS intensity close to $E = 0$ is due to elastic scattering, while the scattering at $E \gtrsim 5$ meV is dominantly due to phonon excitations, as it increases with increasing scattering vector Q and increasing temperature (Supplementary Fig. 6a,b), as well as exhibits typical phonon dispersion arcs extending up to ~40 meV. This signal is practically identical to that obtained from the non-magnetic analogue LaTa$_7$O$_{19}$ (Supplementary Fig. 6c,d). However, in NdTa$_7$O$_{19}$ we find three additional, very flat excitation bands at low Q values, two stronger ones at 9.4 and 38 meV (highlighted by arrows in Fig. 3a) and a weaker one at 87 meV (Fig. 3c and Supplementary Fig. 5a,b), which we attribute to CEF transitions. The low-lying magnetic modes are clearly seen in Fig. 3b where the phonon signal measured in the non-magnetic LaTa$_7$O$_{19}$ is subtracted from the INS intensity of NdTa$_7$O$_{19}$ at 5 K.

In contrast to the phonon modes, the CEF modes become weaker with increasing Q due to decreasing magnetic form factor $F(Q)^2$ of Nd^{3+} ions (inset in Fig. 3c) and lose their intensity at higher temperatures (Supplementary Fig. 6b), as expected for a magnetic signal.

The composition of the CEF states and their corresponding magnetic characteristics follow from a simultaneous CEF fit (Methods) of the INS data (Fig. 3c), the temperature dependence of the magnetic susceptibility (Fig. 2a) and magnetization data at various temperatures (Fig. 2c). The CEF fit predicts that two energy levels almost coincide (Fig. 1c), effectively yielding three CEF transitions between the ground state Kramers doublet and the four excited Kramers doublets of the $^4I_{9/2}$ Nd^{3+} multiplet split by the CEF, as observed in the INS experiment. A very similar situation was encountered in the pyrochlore compound Nd$_2$Zr$_2$O$_7$, where Nd^{3+} ions are also eight-fold coordinated by O^{2-} (ref. [36]). As the first excited doublet lies at an energy gap $\Delta_{CEF} = 9.4$ meV above the ground state, NdTa$_7$O$_{19}$ can be considered an effective spin-1/2 system at temperatures $T \ll \Delta_{CEF}/k_B = 109$ K, where k_B is the Boltzmann constant. The magnetic character of the derived CEF ground state is highly anisotropic, which reflects in anisotropic g factors $g_z = 2.78$ and $g_{xy} = 1.22$ (equation (4)) for the parallel and perpendicular directions, respectively, with respect to the crystallographic c axis. This sets a magnetic easy axis perpendicular to the triangular planes, with the projection of the magnetic moment on the easy axis $\mu_z = g_z\mu_B/2 = 1.39\mu_B$ being rather small. This explains the large reduction of the effective magnetic moment compared to the full free-ion value, which we obtain from the low-temperature CW fit of the magnetic susceptibility (Fig. 2b). As the agreement of the non-interacting CEF model with bulk magnetization data is very good even for $T \ll \Delta_{CEF}/k_B$ (Fig. 2c), the magnetism of NdTa$_7$O$_{19}$ is predominantly determined by CEF effects. So, any exchange interactions between effective spins $S = 1/2$ in the CEF ground state must be small. This is in line with $\theta_{CW}^l = -0.46(3)$ K, which suggests the presence of antiferromagnetic exchange interactions on the order of a kelvin. We note that the pure non-interacting Curie model with $\theta_{CW} = 0$ fits the low-temperature experimental susceptibility
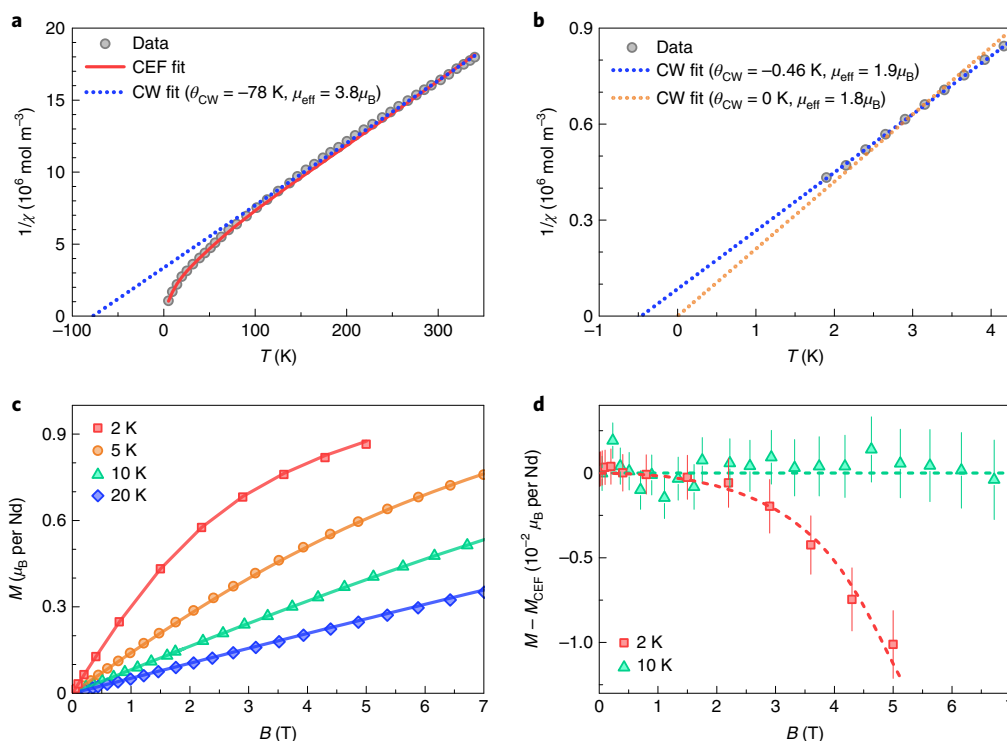
Fig. 2 | Bulk magnetic properties of NdTa$_7$O$_{19}$. a,b, Inverse magnetic susceptibility (without diamagnetic contribution; Methods) in a magnetic field of 100 mT suggests the absence of any magnetic instabilities in NdTa$_7$O$_{19}$ at least down to 1.9 K. The dotted lines correspond to the CW model and indicate small exchange interactions on the order of a kelvin in the CEF ground state (**b**). This agrees well with an excellent fit of a non-interacting CEF model (Methods) to the magnetic susceptibility in the whole temperature range (solid curve in **a**). **c,d,** The CEF model (solid lines) also explains well the magnetic-field dependence of magnetization (*M*) measured at several different temperatures. Deviations from this model are found only at the lowest temperature of 2 K and are highlighted in **d**, where the dashed lines serve as a guide to the eye to emphasize the difference between the experimental magnetization and that of the CEF model (M_{CEF}). Error bars represent an uncertainty of one standard deviation.

notably worse (Fig. 2b), which corroborates the observation that the non-interacting CEF model cannot perfectly describe the experimental magnetization curves at low temperatures, for example, at 2 K in Fig. 2d.

A more quantitative insight into exchange interactions in the ground-state Kramers doublet of NdTa$_7$O$_{19}$ is obtained from electron spin resonance (ESR) measurements (Methods). This method directly measures *g* factors and thus also serves to verify the predictions of the CEF model. The ESR spectrum at 10 K reveals *g*-factor eigenvalues $g_1 = 2.49$, $g_2 = 1.24$ and $g_3 = 1.02$ (Fig. 4a). Considering that the *g* factors of Nd^{3+} ions depend dramatically on the CEF parameters[37], these values are in good agreement with those predicted by our CEF modelling, $g_z = 2.78 \approx g_1$ and $g_{xy} = 1.22 \approx g_2$ and g_3. The small difference between g_2 and g_3 suggests a tiny deviation from the three-fold rotational symmetry at the Nd^{3+} site (Methods), which is below the sensitivity of scattering techniques. A similar situation was observed also in the quantum kagome antiferromagnet herbertsmithite[38].

The ESR line-width δ of the g_1 signal exhibits pronounced temperature dependence and saturates at a constant value $\delta_0 = 0.48(1)$ T below ~10 K (Fig. 4b). This temperature variation is attributed to the Orbach mechanism (Methods) accounting for two-phonon scattering via excited CEF levels and shows a gapped behaviour with an energy gap Δ_{ESR} expected to be on the order of the CEF gap to the lowest excited Kramers doublet[37]. Indeed, we find a reasonably good agreement between $\Delta_{ESR} = 6.5(5)$ meV and $\Delta_{CEF} = 9.4$ meV obtained from INS measurements. The low-temperature saturation value of the ESR line-width $\delta_0 = 0.48(1)$ T is used to assess the exchange

interactions and their anisotropy in the CEF ground state. The broadening due to dipolar interactions amounts to only about ~5 mT and is thus negligible. The experimental line-width can only be explained by strong exchange anisotropy, which is indeed expected for RE-based magnets[37]. It arises from projecting the intrinsic isotropic exchange interaction $\mathcal{J}_0$ between spin degrees of freedom onto the effective $S = 1/2$ spin–orbit-entangled degrees of freedom of the ground-state Kramers doublet, leading to exchange-interaction components[37] $\mathcal{J}_\alpha = \mathcal{J}_0 g_\alpha^2 (g_J - 1)^2 / g_J^2$, where $\alpha = x, y, z$ and $g_J = 8/11$ is the Landé factor of Nd^{3+}. As the in-plane exchange anisotropy is much smaller than the out-of-plane anisotropy, $(\mathcal{J}_y - \mathcal{J}_x)/(\mathcal{J}_z - \mathcal{J}_x) = (g_2^2 - g_3^2)/(g_1^2 - g_3^2) \lesssim 0.1$, we neglect the former and consider an Ising-like spin Hamiltonian

$$\mathcal{H}_{ex} = \sum_{\langle i,j \rangle} \mathcal{J}_z S_i^z S_j^z + \mathcal{J}_{xy} \left(S_i^x S_j^x + S_i^y S_j^y \right)$$
$$= \sum_{\langle i,j \rangle} \left[\left(\mathcal{J} - \tfrac{1}{2} D \right) \left(\mathbf{S}_i \cdot \mathbf{S}_j \right) + \tfrac{3}{2} D S_i^z S_j^z \right] \quad (1)$$

to describe the magnetism of the CEF ground state. Here the sum runs over the nearest-neighbour spins $\mathbf{S}_i$ and $\mathbf{S}_j$ at sites *i* and *j* on the triangular lattice, $\mathcal{J}$ is the isotropic part of the exchange interaction and *D* is the anisotropic part described by a traceless tensor, yielding $\mathcal{J}_z = \mathcal{J} + D$ and $\mathcal{J}_{xy} = \mathcal{J} - D/2$. The anisotropic exchange interaction is evaluated as $D = \sqrt{8/27} g_z \mu_B \delta_0 / k_B = 0.49(1)$ K (equation (7)), which then yields the isotropic exchange interaction $\mathcal{J} = D \left(g_z^2/2 + g_{xy}^2 \right) / \left(g_z^2 - g_{xy}^2 \right) = 0.86 D = 0.41(1)$ K. NdTa$_7$O$_{19}$ is thus a strongly anisotropic spin-1/2 Ising-like TAFM,
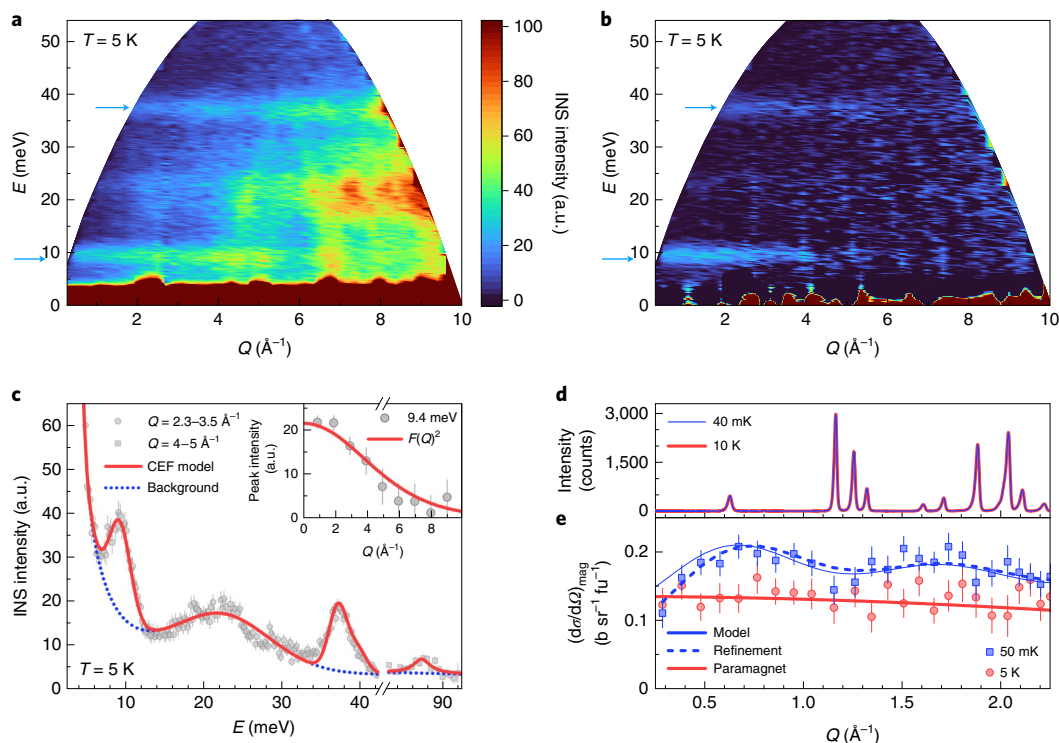
Fig. 3 | Excitations and correlations in NdTa$_7$O$_{19}$. a, INS intensity at 5 K for the neutron incident energy of 60 meV reveals the predominance of phonon excitations at larger scattering vectors Q. **b**, Additional flat bands at low Q values (indicated by arrows) remain present if the INS signal of the non-magnetic analogue LaTa$_7$O$_{19}$ (Supplementary Fig. 6c) is subtracted. These flat modes correspond to CEF magnetic excitations. **c**, Constant-Q cuts (symbols) obtained by integrating the INS data of NdTa$_7$O$_{19}$ over the ranges 2.3–3.5 Å^{-1} and 4–5 Å^{-1} at low and high energy transfers, respectively, are compared to the CEF model including background (solid line). The background (dashed line) is fitted by three Gaussian functions: two centred at $E = 0$ (a narrow one accounts for elastic scattering while a broad one originates from phonons) and another one at ~23 meV that is also due to phonons. The inset shows good agreement of the 9.4 meV CEF peak intensity with the magnetic form factor (solid line). The experimental points are obtained from the difference plot (**b**) by integrating the data in the energy range ±1 meV and averaging over 1-Å^{-1}-wide intervals. **d**, A comparison of neutron diffraction patterns at 40 mK and 10 K reveals the absence of magnetic Bragg peaks even at the lowest experimentally accessible temperature. **e**, The magnetic neutron scattering differential cross-section (($d\sigma/d\Omega)_{mag}$) shows paramagnetic behaviour at 5 K and unveils diffuse scattering due to nearest-neighbour antiferromagnetic spin correlations predominantly of the Ising type at 50 mK. These correlations are modelled using an analytical model as well as reverse Monte Carlo refinements (see Methods for details). Error bars represent an uncertainty of one standard deviation. a.u., arbitrary units; b, barns; fu, formula unit.
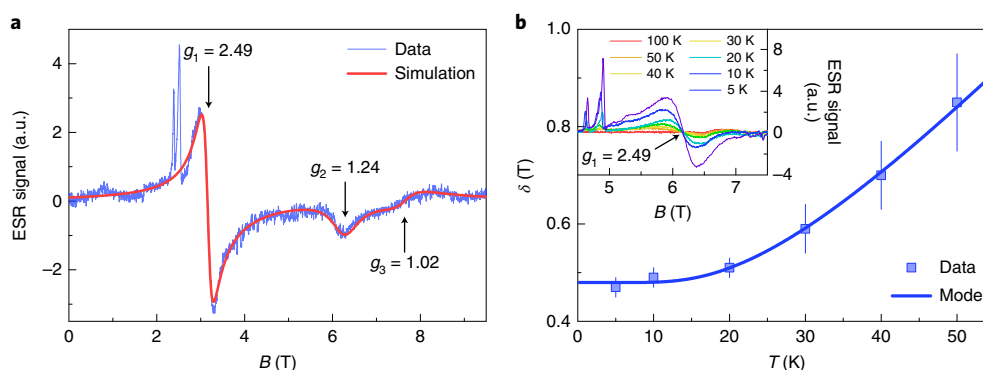

Fig. 4 | Magnetic anisotropy in NdTa$_7$O$_{19}$. a, The ESR spectrum recorded at 109 GHz and 10 K shows broad features at g factors $g_1 = 2.49$, $g_2 = 1.24$ and $g_3 = 1.02$ and is well accounted for by a powder-spectrum simulation (Methods). This corresponds well to the g factors $g_z = 2.78$ and $g_{xy} = 1.22$ obtained from CEF modelling assuming uniaxial asymmetry. A couple of additional, narrow impurity signals are detected, which, however, have orders-of-magnitude smaller intensities than the main broad lines. **b**, The temperature dependence of the peak-to-peak ESR line-width (main panel) of the g_1 component recorded at 211.9 GHz (inset) is explained by the Orbach model of equation (5), while the large low-temperature saturation value of the line-width is accounted for by a large exchange anisotropy. Error bars represent an uncertainty of one standard deviation.

with $\mathcal{J}_z = 0.90(2)$ K and $\mathcal{J}_{xy} = 0.16(2)$ K. The magnitude of the estimated exchange interactions predicts the powder-averaged CW temperature $\theta_{CW} = -3\bar{\mathcal{J}}/2 = -0.62(2)$ K, where $\bar{\mathcal{J}} = (\mathcal{J}_z + 2\mathcal{J}_{xy})/3$ is the average exchange constant. This agrees with the low-temperature CW temperature $\theta_{CW}^l = -0.46(3)$ K determined from bulk magnetic susceptibility.
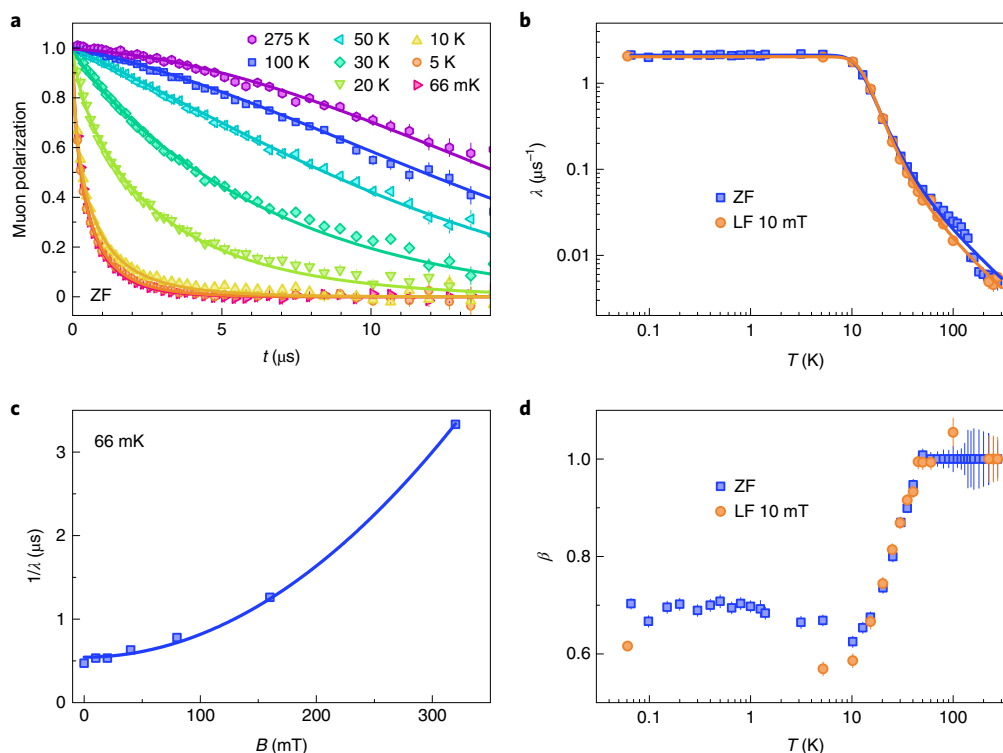
Fig. 5 | Quantum SL ground state of NdTa$_7$O$_{19}$ evidenced by muon spectroscopy. a, Monotonic muon-polarization decay over time t is observed in zero applied magnetic field (ZF) at all temperatures, which reveals the absence of any magnetic ordering or freezing down to at least 66 mK. The solid lines correspond to fits with equation (8). **b,d**, The μSR rates λ due to dynamical local fields (**b**) and corresponding stretching exponents β (**d**) are obtained from these fits for ZF, as well as for a small longitudinal field (LF) of 10 mT. The temperature dependence of λ follows the Orbach model (solid lines) of equation (10). **c**, The $1/\lambda$ measured at 66 mK as a function of the longitudinal magnetic field (B) follows the Redfield model of equation (9) corresponding to fast spin fluctuations. Error bars represent an uncertainty of one standard deviation.

Since the magnetic interactions in NdTa$_7$O$_{19}$ are rather small, determination of its magnetic ground state requires investigation at millikelvin temperatures. Neutron diffraction (Methods) shows no sign of magnetic Bragg peaks even at the base temperature of 40 mK. In fact, the diffraction pattern remains the same as that measured at 10 K (Fig. 3d; for a difference plot, Supplementary Fig. 7c). Furthermore, polarized neutron scattering measurements (Methods) reveal magnetic diffuse scattering (Fig. 3e). At 5 K, this scattering is explained well with a parameter-free paramagnetic model (Methods). Most importantly, at 50 mK, the magnetic diffuse scattering gets enhanced and develops oscillations (Fig. 3e). Their period corresponds well to the nearest-neighbour Nd–Nd distance, while their shape and the overall enhancement of the signal reveals the antiferromagnetic and predominantly Ising nature of the spin correlations; that is, the correlations are about four times stronger along the c axis than along the other two, perpendicular directions (Methods for quantitative modelling).

For a complementary proof of a magnetically disordered ground state, we resort to muon spin relaxation (μSR) spectroscopy (Methods), a technique that provides a very sensitive local probe of internal magnetic fields[39]. These measurements indeed unambiguously confirm a dynamical ground state. Namely, down to the lowest experimental temperature of $T = 66$ mK $\ll \mathcal{J}_z$, the muon polarization remains a monotonically decaying function (Fig. 5a), which is a hallmark of the dynamical local fields of electronic origin present at the muon stopping site[39]. Static internal magnetic fields, by contrast, would result in coherent oscillations of the muon polarization.

The μSR rate λ due to dynamical local fields (Methods) remains constant up to around 10 K and then starts decreasing profoundly

with increasing temperature (Fig. 5b). Such temperature dependence corresponds to the presence of two relaxation mechanisms—a temperature-independent one, characteristic of the CEF ground-state Kramers doublet, and a thermally activated one that prevails at higher temperatures (equation (10)). As with the ESR line-width, we find that the temperature dependence of λ is due to the Orbach process, yielding the energy gap $\Delta_{\mu SR} = 5.7(5)$ meV, which is in very good agreement with the estimate $\Delta_{ESR} = 6.5(5)$ meV from ESR. We note that a very similar behaviour with a low-temperature relaxation plateau was found also in Nd-based langasite featuring a frustrated kagome lattice[40], as well as in a few other RE-based frustrated magnets[22,41,42]. Although the plateau is typically regarded as a fingerprint of a correlated magnetically disordered ground state, in NdTa$_7$O$_{19}$ it apparently does not originate from spin correlations, which are absent at 5 K (Fig. 3e).

A further insight into spin fluctuations characteristic of the disordered magnetic ground state of NdTa$_7$O$_{19}$ is provided by the field dependence of the μSR rate at the plateau. The measurements performed at 66 mK (Fig. 5c) show that the system is in the fast-fluctuation regime as λ obeys the Redfield relation of equation (9). Namely, the fit to the data yields the width of the local-field distribution at the muon stopping site $B_{loc} = 12(1)$ mT and the corresponding spin fluctuation frequency $\nu_e = 120(10)$ MHz $\gg \gamma_\mu B_{loc} = 10$ MHz, where $\gamma_\mu = 851.616$ MHz/T is the muon gyromagnetic ratio. While the derived B_{loc} is comparable to typical values of fluctuating magnetic fields at muon stopping sites in insulating oxides[39], ν_e is very small compared to the frequency of exchange fluctuations, $k_B \bar{\mathcal{J}}/\hbar \simeq 50$ GHz, where $\hbar$ is the reduced Planck constant implying that a simple paramagnetic picture with field-independent ν_e does not apply. The ground state in NdTa$_7$O$_{19}$ is essentially different from

that observed in the Ising pyrochlore compound $Nd_2Zr_2O_7$, where the dynamics coexist with static order as $\nu_e \approx \gamma_\mu B_{loc}$ (ref. [43]) and magnetic Bragg peaks are present[36]. The absence of these in $NdTa_7O_{19}$ (Fig. 3d) indicates that potential static correlations appear on timescales shorter than 10^{-12} s. Finally, we note that since the ground state of $NdTa_7O_{19}$ is characterized by strong magnetic anisotropy, a strongly orientation-dependent decay of temporal spin correlations should reflect in a broad distribution of μSR rates in a polycrystalline sample. Indeed, this is observed experimentally via a pronounced decrease of the stretching exponent β (Fig. 5d) characterizing the decay of the muon polarization (Methods), from the high-temperature value of 1 to 0.68(3) at low temperatures. This corresponds to a strong widening of the distribution of λ in the magnetic ground state.

Having established $NdTa_7O_{19}$ as a RE-based TAFM compound with a SL ground state, we next compare it to the most intensively investigated example of this model—the $YbMgGaO_4$ compound. We first note that the two systems behave very similarly. Just as in $NdTa_7O_{19}$, also in $YbMgGaO_4$ the μSR rate exhibits a low-temperature plateau and is characterized by a decrease in the stretching exponent when entering the low-temperature region[22]. Furthermore, the CW temperature of the latter compound is also on the order of 1 K and the ESR line-width is very similar to the one we found in $NdTa_7O_{19}$ (ref. [20]), suggesting that the two systems have similarly strong exchange anisotropies. Nevertheless, we stress that in $NdTa_7O_{19}$, the dominant anisotropy is of the Ising type with $\mathcal{J}_z/\mathcal{J}_{xy} = 5.6$, while in $YbMgGaO_4$ it is of the easy-plane type with $\mathcal{J}_z/\mathcal{J}_{xy} = 0.5$ (ref. [20]). On the other hand, related RE-based delafossites $ErMgGaO_4$ (ref. [44]) and $TmMgGaO_4$ (ref. [45]) possess Ising anisotropy, but are, like $YbMgGaO_4$, hampered by RE positional disorder and Ga/Mg site mixing, which lead to inhomogeneous magnetism and even partial magnetic order in the latter case. Magnetic ordering occurs also in strongly anisotropic Ising TAFM compounds $ACoX_2$ (A = Cs, Rb; X = Cl, Br) with $\mathcal{J}_z/\mathcal{J}_{xy} \approx 10$, where, however, interlayer coupling $(\mathcal{J}')$ is sizeable, $\mathcal{J}'/\mathcal{J}_z \approx 0.1$ (ref. [46]). The discovery that $NdTa_7O_{19}$ is a disorder-free Ising-like TAFM with a dynamical ground state thus makes this compound unique, as it contrasts with other well-studied systems. Finally, we note that even though our lowest experimental temperature $T_0 = 40$ mK is not extremely small compared to $\mathcal{J}_z$, that is, $T_0/\mathcal{J}_z = 0.044$, it is enough to distinguish our system from the symmetric Heisenberg TAFM where long-range order sets in at the Néel temperature T_N already at $T_N/\mathcal{J} \geq 0.044$ for the tiniest interlayer interactions $\mathcal{J}'/\mathcal{J} \gtrsim 10^{-18}$ (refs. [47,48]).

The magnetically disordered ground state of $NdTa_7O_{19}$ is attributed to the dominant Ising character of the nearest-neighbour exchange interaction and is observed in the absence of structural disorder, contrary to previous cases[23–26]. The Ising interaction $\mathcal{J}_z$ acts between the effective spin-1/2 spin–orbit-entangled degrees of freedom within the CEF ground-state Kramers doublet. The observed low-frequency excitations, persisting to the lowest temperatures, reveal a potentially crucial role of an additional non-commuting exchange interaction $\mathcal{J}_{xy}$ that lifts the degeneracy of the classical Ising model and introduces quantum dynamics[14], which can be understood within the famous resonating-valence-bond scenario suggested by Fazekas and Anderson[7,16]. A similar mechanism is responsible for stabilization of a quantum SL phase of pyrochlores known as quantum spin ice[5,49] and thus appears to be universal among various highly anisotropic frustrated spin lattices. Our results open an alternative perspective for modern theoretical approaches, which have so far focused on unconventional phases in the easy-plane region of the TAFM phase diagram[12]. The effect of anisotropy in the TAFM model could be investigated more thoroughly experimentally by inspecting various members of the large family of RE heptatantalates and other related RE-based TAFM compounds. These quantum materials provide an optimal framework for realizations of quantum SLs borne out of magnetic anisotropy, similarly as observed in the paradigmatic Kitaev honeycomb model[50]. Such states are also of high technological relevance, as they represent a promising platform for quantum computing.

Online content

Any methods, additional references, Nature Research reporting summaries, source data, extended data, supplementary information, acknowledgements, peer review information; details of author contributions and competing interests; and statements of data and code availability are available at https://doi.org/10.1038/s41563-021-01169-y.

References

1. Basov, D., Averitt, R. & Hsieh, D. Towards properties on demand in quantum materials. *Nat. Mater.* **16**, 1077–1088 (2017).
2. Keimer, B. & Moore, J. E. The physics of quantum materials. *Nat. Phys.* **13**, 1045–1055 (2017).
3. Tokura, Y., Kawasaki, M. & Nagaosa, N. Emergent functions of quantum materials. *Nat. Phys.* **13**, 1056–1068 (2017).
4. Balents, L. Spin liquids in frustrated magnets. *Nature* **464**, 199 (2010).
5. Savary, L. & Balents, L. Quantum spin liquids: a review. *Rep. Prog. Phys.* **80**, 016502 (2017).
6. Broholm, C. et al. Quantum spin liquids. *Science* **367**, eaay0668 (2020).
7. Anderson, P. W. Resonating valence bonds: a new kind of insulator? *Mater. Res. Bull.* **8**, 153–160 (1973).
8. Capriotti, L., Trumper, A. E. & Sorella, S. Long-range Néel order in the triangular Heisenberg model. *Phys. Rev. Lett.* **82**, 3899 (1999).
9. Iqbal, Y., Hu, W.-J., Thomale, R., Poilblanc, D. & Becca, F. Spin liquid nature in the Heisenberg $J_1 − J_2$ triangular antiferromagnet. *Phys. Rev. B* **93**, 144411 (2016).
10. Yunoki, S. & Sorella, S. Two spin liquid phases in the spatially anisotropic triangular Heisenberg model. *Phys. Rev. B* **74**, 014408 (2006).
11. Yamamoto, D., Marmorini, G. & Danshita, I. Quantum phase diagram of the triangular-lattice *xxz* model in a magnetic field. *Phys. Rev. Lett.* **112**, 127203 (2014).
12. Maksimov, P. A., Zhu, Z., White, S. R. & Chernyshev, A. L. Anisotropic-exchange magnets on a triangular lattice: spin waves, accidental degeneracies, and dual spin liquids. *Phys. Rev. X* **9**, 021017 (2019).
13. Wannier, G. H. Antiferromagnetism. The triangular Ising net. *Phys. Rev.* **79**, 357 (1950).
14. Moessner, R. & Sondhi, S. L. Ising models of quantum frustration. *Phys. Rev. B* **63**, 224401 (2001).
15. Nagai, O., Horiguchi, T. & Miyashita, S. in *Frustrated Spin Systems* (ed. Diep, H. T.) (World Scientific, 2004).
16. Fazekas, P. & Anderson, P. W. On the ground state properties of the anisotropic triangular antiferromagnet. *Philos. Mag.* **30**, 423 (1974).
17. Li, Y.-D., Wang, X. & Chen, G. Anisotropic spin model of strong spin-orbit-coupled triangular antiferromagnets. *Phys. Rev. B* **94**, 035107 (2016).
18. Iaconis, J., Liu, C., Halász, G. B. & Balents, L. Spin liquid versus spin orbit coupling on the triangular lattice. *SciPost Phys.* **4**, 003 (2018).
19. Witczak-Krempa, W., Chen, G., Kim, Y. B. & Balents, L. Correlated quantum phenomena in the strong spin-orbit regime. *Annu. Rev. Condens. Matter Phys.* **5**, 57–82 (2014).
20. Li, Y. et al. Rare-earth triangular lattice spin liquid: a single-crystal study of $YbMgGaO_4$. *Phys. Rev. Lett.* **115**, 167203 (2015).
21. Shen, Y. et al. Evidence for a spinon Fermi surface in a triangular-lattice quantum-spin-liquid candidate. *Nature* **540**, 559–562 (2016).
22. Li, Y. et al. Muon spin relaxation evidence for the U(1) quantum spin-liquid ground state in the triangular antiferromagnet $YbMgGaO_4$. *Phys. Rev. Lett.* **117**, 097201 (2016).
23. Zhu, Z., Maksimov, P. A., White, S. R. & Chernyshev, A. L. Disorder-induced mimicry of a spin liquid in $YbMgGaO_4$. *Phys. Rev. Lett.* **119**, 157201 (2017).
24. Kimchi, I., Nahum, A. & Senthil, T. Valence bonds in random quantum magnets: theory and application to $YbMgGaO_4$. *Phys. Rev. X* **8**, 031028 (2018).
25. Watanabe, K., Kawamura, H., Nakano, H. & Sakai, T. Quantum spin-liquid behavior in the spin-1/2 random Heisenberg antiferromagnet on the triangular lattice. *J. Phys. Soc. Jpn* **83**, 034714 (2014).
26. Kawamura, H. & Uematsu, K. Nature of the randomness-induced quantum spin liquids in two dimensions. *J. Phys. Condens. Matter* **31**, 504003 (2019).

27. Shimizu, Y., Miyagawa, K., Kanoda, K., Maesato, M. & Saito, G. Spin liquid state in an organic Mott insulator with a triangular lattice. *Phys. Rev. Lett.* **91**, 107001 (2003).

28. Itou, T., Oyamada, A., Maegawa, S., Tamura, M. & Kato, R. Quantum spin liquid in the spin-1/2 triangular antiferromagnet EtMe$_3$Sb[Pd(dmit)$_2$]$_2$. *Phys. Rev. B* **77**, 104413 (2008).

29. Klanjšek, M. et al. A high-temperature quantum spin liquid with polaron spins. *Nat. Phys.* **13**, 1130–1134 (2017).

30. Liu, W. et al. Rare-earth chalcogenides: a large family of triangular lattice spin liquid candidates. *Chin. Phys. Lett.* **35**, 117501 (2018).

31. Bordelon, M. M. et al. Field-tunable quantum disordered ground state in the triangular-lattice antiferromagnet NaYbO$_2$. *Nat. Phys.* **15**, 1058 (2019).

32. Ashtar, M. et al. REZnAl$_{11}$O$_{19}$ (RE= Pr, Nd, Sm–Tb): a new family of ideal 2D triangular lattice frustrated magnets. *J. Mater. Chem. C* **7**, 10073 (2019).

33. Schaffrath, U. & Gruehn, R. Zum chemischen transport von verbindungen des typs LnTa$_7$O$_{19}$ (Ln= La–Nd) mit einer bemerkung zur strukturverfeinerung von NdTa$_7$O$_{19}$. *Z. Anorg. Allg. Chem.* **588**, 43–54 (1990).

34. Leonyuk, N. I. et al. A new generation of nonlinear optical and laser crystals of rare earth borate and tantalate families. *J. Optoelectron. Adv. Mater.* **9**, 1206–1214 (2007).

35. Simonet, V. et al. Hidden magnetic frustration by quantum relaxation in anisotropic Nd langasite. *Phys. Rev. Lett.* **100**, 237204 (2008).

36. Xu, J. et al. Magnetic structure and crystal-field states of the pyrochlore antiferromagnet Nd$_2$Zr$_2$O$_7$. *Phys. Rev. B* **92**, 224430 (2015).

37. Abragam, A. & Bleaney, B. *Electron Paramagnetic Resonance of Transition Ions* (Clarendon Press, 1970).

38. Zorko, A. et al. Symmetry reduction in the quantum kagome antiferromagnet herbertsmithite. *Phys. Rev. Lett.* **118**, 017202 (2017).

39. Yaouanc, A. & De Réotier, P. D. *Muon Spin Rotation, Relaxation, and Resonance: Applications to Condensed Matter* (Oxford Univ. Press, 2011).

40. Zorko, A. et al. Easy-axis kagome antiferromagnet: local-probe study of Nd$_3$Ga$_5$SiO$_{14}$. *Phys. Rev. Lett.* **100**, 147201 (2008).

41. Gardner, J. S. et al. Cooperative paramagnetism in the geometrically frustrated pyrochlore antiferromagnet Tb$_2$Ti$_2$O$_7$. *Phys. Rev. Lett.* **82**, 1012 (1999).

42. Clark, L. et al. Two-dimensional spin liquid behaviour in the triangular-honeycomb antiferromagnet TbInO$_3$. *Nat. Phys.* **15**, 262–268 (2019).

43. Xu, J., Balz, C., Baines, C., Luetkens, H. & Lake, B. Spin dynamics of the ordered dipolar-octupolar pseudospin-1/2 pyrochlore Nd$_2$Zr$_2$O$_7$ probed by muon spin relaxation. *Phys. Rev. B* **94**, 064425 (2016).

44. Cevallos, F. A., Stolze, K. & Cava, R. J. Structural disorder and elementary magnetic properties of triangular lattice ErMgGaO$_4$ single crystals. *Solid State Commun.* **276**, 5–8 (2018).

45. Li, Y. et al. Partial up-up-down order with the continuously distributed order parameter in the triangular antiferromagnet TmMgGaO$_4$. *Phys. Rev. X* **10**, 011007 (2020).

46. Collins, M. F. & Petrenko, O. A. Triangular antiferromagnets. *Can. J. Phys.* **75**, 605 (1997).

47. Du, A., Li, J. & Wei, G. Z. The Heisenberg model on a stacked-triangular lattice: spin Green function approach. *Phys. Status Solidi B* **240**, 230–239 (2003).

48. Murtazaev, A. K. & Ramazanov, M. K. Critical properties of the three-dimensional frustrated Heisenberg model on a layered-triangular lattice with variable interplane exchange interaction. *Phys. Rev. B* **76**, 174421 (2007).

49. Gingras, M. J. P. & McClarty, P. A. Quantum spin ice: a search for gapless quantum spin liquids in pyrochlore magnets. *Rep. Prog. Phys.* **77**, 056501 (2014).

50. Kitaev, A. Y. Anyons in an exactly solved model and beyond. *Ann. Phys.* **321**, 2–111 (2006).

Methods

Synthesis and crystal structure. A polycrystalline sample of NdTa$_7$O$_{19}$ was prepared by a conventional solid-state synthesis method from high-purity Nd$_2$O$_3$ (Alfa Aesar, 99.994%) and Ta$_2$O$_5$ (Alfa Aesar, 99.993%)[51]. Prior to use, Nd$_2$O$_3$ was preheated at 900 °C for 12 h. Stoichiometric amounts of each material were mixed and pelletized. Single-phase white-coloured NdTa$_7$O$_{19}$ sample was obtained after heat treatment of the reactants for several days at 950 °C, 1,000 °C, 1,050 °C, 1,100 °C, 1,150 °C and 1,200 °C with intermediate grindings. Its phase purity was checked with a Rigaku X-ray diffractometer at room temperature using Cu K$_\alpha$ radiation. The only impurity phase found was 0.2(1) wt% of residual Ta$_2$O$_5$. The Rietveld refinement was carried out within the space group $P\bar{6}c2$ using FullProf Suite[52]. The results are shown in Supplementary Fig. 1 and the parameters are summarized in Supplementary Table I. No anti-site ion disorder or non-stoichiometry was detected in this compound, as confirmed by additional neutron diffraction measurements at 40 mK (Supplementary Fig. 2). This established NdTa$_7$O$_{19}$ as a disorder-free TAFM.

In the unit cell with the $P\bar{6}c2$ symmetry, the magnetic Nd^{3+} ions occupy the 2c Wyckoff position and form an equilateral triangular lattice within the ab crystal plane (Fig. 1). The nearest-neighbour distance between the magnetic ions is 6.224 Å and is much smaller than the interlayer distance of $c/2 = 9.969$ Å. Furthermore, the exchange interaction within the triangular layers is mediated via –O–Ta–O– exchange bridges (Fig. 1b), while –O–Ta–O–Ta–O– bridges that are involved in the interlayer exchange (Fig. 1a) are much longer. Therefore, the deviation of the spin lattice in NdTa$_7$O$_{19}$ from the two-dimensional TAFM model is expected to be very small.

Bulk magnetic measurements. Bulk magnetic measurements were performed on a polycrystalline NdTa$_7$O$_{19}$ sample enclosed in a plastic container. Quantum Design superconducting quantum interference device magnetometers were employed in the temperature range between 1.9 and 340 K and field range up to 7 T. The magnetic susceptibility $\chi = M/H$, where M is sample magnetization, was measured in a magnetic field $\mu_0 H = 100$ mT, with μ_0 being vacuum permeability. The susceptibility of the sample container was measured separately and subtracted from the total susceptibility. Also the diamagnetic susceptibility of the NdTa$_7$O$_{19}$ sample $\chi_{dia} = -4.3 \times 10^{-3}$ cm^3 mol^{-1} (ref. [53]) was subtracted to obtain the paramagnetic susceptibility shown in Fig. 2. Additional control measurements on powder embedded in wax showed that crystallites of NdTa$_7$O$_{19}$ do not align with an external magnetic field.

The obtained χ was compared to the CW model $\chi = C/(T - \theta_{CW})$ in different temperature regions. Here θ_{CW} is the CW temperature and the Curie constant is given by $C = N_A \mu_0 \mu_{eff}^2/(3k_B)$, with N_A, k_B and μ_{eff} being the Avogadro number, the Boltzmann constant and an effective magnetic moment, respectively. The CW fit in the high-temperature region above 100 K (Fig. 2a) yields the CW temperature $\theta_{CW}^h = -78(4)$ K and the effective moment $\mu_{eff}^h = 3.8(1)\mu_B$. The latter is close to the value $g_J \sqrt{J(J+1)}\mu_B = 3.62\mu_B$ expected for a free $^4I_{9/2}$ Nd^{3+} ion. The fit with the same model in the low-temperature region was done systematically by varying the upper and the lower temperature limit of the fitting range, T_{max} and T_{min}, respectively (Supplementary Fig. 3). This allowed us to discard the effects of excited CEF levels on the fit at the high-temperature end and to check for possible spin-correlation effects at the low-temperature end. The fit is independent of the upper limit for $T_{max} \leq 4.2$ K, and the saturated value of the CW temperature is not affected by the lower limit all the way up to $T_{min} = 3.4$ K. The obtained parameters are $\theta_{CW}^l = -0.46(3)$ K and $\mu_{eff}^l = 1.9(1)\mu_B$.

Inelastic neutron scattering. INS measurements were performed using the MARI spectrometer at the ISIS Pulsed Neutron and Muon Source of the Rutherford Appleton Laboratory. The spectrometer has a continuous detector coverage from 3.5–135°. Approximately 5.3 g of polycrystalline NdTa$_7$O$_{19}$ sample was loaded into an aluminium sample holder with an annular geometry. The dynamical structure factor as a function of the scattering wave vector **Q** and energy E, was measured at 5 and 200 K for the incident energies $E = 60$ and 100 meV, selected using a Fermi chopper system with a Gd foil chopper pack rotating at 200 Hz. The chosen configuration of the instrument ensured an elastic line resolution of $\delta E/E \approx 0.04$ and Q ranges of ~0.25–9.5 Å^{-1} and ~0.35–12.7 Å^{-1} for $E = 60$ and 100 meV, respectively. Measurements at the same experimental conditions were also done on the non-magnetic analogue LaTa$_7$O$_{19}$ with a mass of approximately 5.3 g. We note that the magnetic signal of the CEF modes is rather weak compared to the signal of the phonon modes (Fig. 3a and Supplementary Figs. 5 and 6), because the fraction of the magnetic Nd^{3+} ions with respect to all ions in NdTa$_7$O$_{19}$ is only 1:27. Moreover, the highest CEF mode at 87(1) meV is barely noticeable, because the data at this energy start only at $Q = 3.5$ Å^{-1} (Supplementary Fig. 5a,b), where the magnetic form factor is already substantially reduced.

Neutron diffraction. Powder neutron diffraction data were collected on the WISH time-of-flight diffractometer at the ISIS Pulsed Neutron and Muon Source of the Rutherford Appleton Laboratory. Approximately 5.4 g of sample was loaded into a copper cylinder and measured at 40 mK and 10 K. The system preserves the symmetry (space group $P\bar{6}c2$; Supplementary Fig. 2 for Rietveld refinement) found by X-ray diffraction at room temperature. For convenience, the neutron diffraction

data in Fig. 3d are presented as a function of Q extending from 0.2 Å^{-1}, which covers the lowest-Q peaks of potential antiferromagnetic orders within as well as between the planes.

Polarized neutron scattering. Experiments with polarized neutrons were conducted on the D7 diffuse scattering spectrometer at the Institut Laue-Langevin. The measurements were performed on a sample with a mass of 5.4 g at 50 mK and 5 K with neutrons of incident energy 3.55 meV and wavelength 4.8707 Å, allowing measurements in the Q range 0.3–2.5 Å^{-1}. Standard vanadium calibration of detectors and quartz polarization corrections were performed. The three-directional XYZ polarization analysis[54] allowed us to separate the magnetic contribution to the neutron scattering differential cross-section $(d\sigma/d\Omega)_{mag}$ from the incoherent and nuclear coherent contributions (Supplementary Fig. 7a). The diffraction mode of the instrument was used, effectively integrating the scattering intensity up to the neutron incident energy and thus yielding an instantaneous structure factor.

The magnetic scattering differential cross-section displays no sharp peaks, yet it shows broad diffuse magnetic scattering. This is clearly enhanced at 50 mK when compared to the signal at 5 K (Fig. 3e). Moreover, at 50 mK it exhibits oscillations in Q, while a monotonic dependence is found at 5 K. For a magnetically disordered powder sample, the magnetic scattering differential cross-section takes the form[55]

$$\left(\frac{d\sigma}{d\Omega}\right)_{mag} = \left(\frac{\mu_n e^2}{2m_e}\right)^2 g^2 S(S+1) F(Q)^2 \left[\frac{2}{3} + C(Q)\right], \tag{2}$$

where μ_n is the magnetic moment of the neutron, e is the elementary charge and m_e is the electron mass. The constant 2/3 in the square brackets is due to self correlations, while the oscillating term $C(Q)$ becomes non-zero only when correlations develop between neighbouring spins. With no adjustable parameters, we find excellent agreement of the uncorrelated paramagnetic model ($C(Q) = 0$) with measurements at 5 K for the powder-averaged g factor $g_{pwd} = (g_z^2/3 + 2g_{xy}^2/3)^{1/2} = 1.89$ (Fig. 3e). The modulation of diffuse scattering at 50 mK, on the other hand, reveals that correlations develop between nearest neighbours on the triangular lattice, as it corresponds perfectly to the nearest-neighbour distance $r_1 = 6.22$ Å. If these correlations were isotropic, the oscillating term $C(Q) \propto \sin(Qr_1)/(Qr_1)$ would simply be added to the paramagnetic signal[54,55]. However, the sizeable overall increase of the signal at 50 mK when compared to the signal at 5 K reveals that the effective g factor becomes enhanced at low temperatures, signifying that correlations dominantly develop along the direction of the largest g factor, which is perpendicular to the triangular planes. Therefore, we model the experiment assuming Ising correlations perpendicular to nearest-neighbour pairs, for which the spin-correlation term in equation (2) is given by[55]

$$C(Q) = \frac{\langle \mathbf{S}_0 \cdot \mathbf{S}_1 \rangle}{S(S+1)} Z_1 \left[\frac{\sin(Qr_1)}{Qr_1} + \frac{\cos(Qr_1)}{(Qr_1)^2} - \frac{\sin(Qr_1)}{(Qr_1)^3}\right], \tag{3}$$

where $Z_1 = 6$ stands for the number of nearest neighbours on the triangular lattice. The fit (Fig. 3e) yields an effective g factor of 2.31 and an average correlation of $Z_1 \langle \mathbf{S}_0 \cdot \mathbf{S}_1 \rangle /S(S+1) = -0.37$.

The predominantly Ising nature of spin correlations in NdTa$_7$O$_{19}$ at 50 mK was verified with reverse Monte Carlo refinements using SPINVERT suite[55]. A spin supercell of 3×3 unit cells was fitted to experimental diffuse scattering, in order to limit the correlations to nearest neighbours, as the experimental data are too noisy to allow for accurate determination of further neighbour correlations. Refinements were performed for 300 proposed reorientations per spin, which ensured good convergence of χ^2. A total of 216 independent spin configurations were calculated in order to obtain good statistics. The spins were chosen to be either one dimensional (1D; Ising type) or three dimensional (3D; Heisenberg type). For 1D spins, the refinements gave identical results to the analytical model of equation (3) (Supplementary Fig. 7b), demonstrating that the reverse Monte Carlo approach works very well in NdTa$_7$O$_{19}$. Refinements with 3D spins were performed to verify the suitability of the Ising picture. For each configuration of 3D spins, we first determined the preferred spin direction, on which the sum of absolute spin projections was maximal. Then, parallel spin correlations $\langle \mathbf{S}_{0,\parallel} \cdot \mathbf{S}_{1,\parallel} \rangle$ and transverse spin correlations $\langle \mathbf{S}_{0,\perp} \cdot \mathbf{S}_{1,\perp} \rangle$ between nearest neighbours were calculated averaging over all 9×216 spins. Refinements with 3D spins yielded a notably better agreement with the experiment than with 1D spins (Fig. 3e), as the corresponding χ^2 was reduced from 18.8 to 13.1. Nevertheless, we find that the parallel correlations $Z_1 \langle \mathbf{S}_{0,\parallel} \cdot \mathbf{S}_{1,\parallel} \rangle/S(S+1) = -0.40(12)$ are almost the same as in the pure Ising (1D) picture, while additional transverse correlations $\frac{1}{2} Z_1 \langle \mathbf{S}_{0,\perp} \cdot \mathbf{S}_{1,\perp} \rangle/S(S+1) = -0.09(6)$ for each of the two perpendicular directions are much smaller, in agreement with $\mathcal{J}_{xy}/\mathcal{J}_z = 0.18$.

CEF modelling. The five CEF Kramers doublets can be written as linear combinations of the eigenstates $|\pm m_J\rangle$ of the z component of the total-spin operator, where $m_J = (2n-1)/2$, $n = 1$–5. The composition of these states depends on the CEF Hamiltonian $\mathcal{H}_{CEF} = \sum_{l,m} B_l^m O_l^m$, where O_l^m are Stevens operators[56] and B_l^m are the corresponding scaling parameters. In order to determine these parameters, allowed by the Nd^{3+} site point symmetry in NdTa$_7$O$_{19}$ with a

dihedral D_3 group, we simultaneously fitted the INS data (Fig. 3c; the width of the CEF peaks of ~2.5 meV is determined by instrumental resolution), magnetic susceptibility data (Fig. 2a) and magnetization data (Fig. 2c) using MANTID software[57]. The combined fit agrees well with all experiments and yields the B_l^m parameters summarized in Supplementary Table II. We note that the parameters substantially deviate from those predicted by the point-charge model (Supplementary Table II), as often found in RE-based systems[58].

The estimated B_l^m parameters predict the five Kramers doublets given in Supplementary Table III and with corresponding energies visualized in Fig. 1c. All four transitions from the CEF ground state to the excited states occur for energy transfers below 100 meV, which is covered by our INS experiments. However, only three flat INS modes are observed experimentally, because the energies of two excited states almost coincide and yield a single broad peak at 38 meV. Knowing the composition of the CEF ground state allows us to determine the corresponding g-factor anisotropy[37]:

$$g_z = 2g_J |\langle \pm\omega_0 |J_z| \pm \omega_0 \rangle| = 2.78,$$
$$g_{xy} = g_J |\langle \pm\omega_0 |J_\pm| \mp \omega_0 \rangle| = 1.22, \qquad (4)$$

where z and xy denote directions parallel and perpendicular, respectively, to the crystallographic c axis that is perpendicular to the triangular layers and $\pm\omega_0$ is the ground-state Kramers doublet (Supplementary Table III). To account for the splitting of g_{xy} into $g_2 = 1.24$ and $g_3 = 1.02$, as observed by ESR (Fig. 4a), an additional, symmetry-lowering CEF term is required; for example, a tiny term $B_6^4 \simeq -0.00005$ meV reproduces this splitting while leaving the energies of the Kramers doublets as well as other experimental observables almost unchanged.

ESR. ESR measurements were performed at the National High Magnetic Field Laboratory on a custom-made transmission-type ESR spectrometer with homodyne detection equipped with a sweepable 15 T superconducting magnet. The measurements were performed in the Faraday configuration at the irradiation frequencies of 109 and 211.9 GHz on a 200 mg polycrystalline sample in a Teflon container. The temperature was controlled using a continuous-flow He cryostat in the temperature range between 5 and 100 K. A standard field-modulation technique was used with the modulation field of about 2 mT to enhance the signal-to-noise ratio.

The spectra consist of intrinsic broad features and a couple of extrinsic narrow lines that are due to impurities and have much lower intensities. The spectrum recorded at 109 GHz and 10 K (Fig. 4a) that shows three intrinsic features of different shapes was simulated by assuming isotropic powder distribution and angular-dependent g factor $g = (g_1^2\cos^2\theta + g_2^2\sin^2\theta\sin^2\phi + g_3^2\sin^2\theta\cos^2\phi)^{1/2}$. Here, θ and ϕ are the polar and the azimuthal angle, respectively, which define the direction of the external magnetic field in the eigenframe of the g tensor. A convolution was performed with a Lorentzian lineshape with angle-dependent line-width and phase between dispersion and absorption, which is arbitrary in our experiment. The fit yields the phase of 72°; g-factor eigenvalues $g_1 = 2.49$, $g_2 = 1.24$ and $g_3 = 1.02$; and about 2.5 times smaller line-width in the direction of g_1 than in the other two directions.

The temperature dependence of the ESR line-width (Fig. 4b) of the g_1 line obeys the relation

$$\delta(T) = \delta_0 + \frac{a}{\exp(\Delta_{ESR}/T) - 1}. \qquad (5)$$

The constant δ_0 term is attributed to magnetic anisotropy in the ground-state Kramers doublet, while the exponential term describes the Orbach relaxation process arising from CEF fluctuations due to two-phonon scattering via intermediate CEF states[37]. In this process, the spin fluctuation frequency dramatically increases with temperature due to increasing phonon density

$$\nu_e \propto 1/\left[\exp\left(\Delta/k_B T\right) - 1\right], \qquad (6)$$

causing ESR line broadening. The fit to the experimental data yields the energy gap $\Delta_{ESR} = 6.5(5)$ meV, the scaling constant $a = 1.3(1)$ T and the zero-temperature line-width $\delta_0 = 0.48(1)$ T.

In the first approximation, that is, neglecting exchange-narrowing effects, the zero-temperature ESR line-width is given by

$$\delta_0 = \sqrt{M_2}/g\mu_B, \qquad (7)$$

where $M_2 = \frac{1}{3} zS(S+1)(3D/2)^2$ is the second moment of the absorption line[37] and $z = 6$ denotes the number of nearest neighbours on the triangular lattice. We stress that the estimated exchange anisotropy is stronger than the isotropic exchange interaction, $D > J$ (main text), which justifies omission of the exchange-narrowing effects[37].

The μSR. The μSR measurements were performed on the MUSR spectrometer at the ISIS Pulsed Neutron and Muon Source of the Rutherford Appleton Laboratory. About 1 g of polycrystalline sample was put on a silver sample holder and was covered by diluted GE varnish to ensure good thermal conductivity at millikelvin temperatures. The experiment was performed in zero field and in various longitudinal fields in the

temperature range between 66 mK and 275 K. A dilution-refrigerator set-up was used to reach the lowest temperatures, while a standard He-flow cryostat was used for temperatures above 2 K. Several runs at the same experimental conditions were done to calibrate the data between the two set-ups.

As muons stopping in the sample are initially almost fully polarized, the time dependence of their polarization $P(t)$ provides an extremely sensitive probe of local magnetic fields[39]. The experimentally measured muon asymmetry is proportional to the muon polarization, $A(t) = A_0 P(t) + A_{bgd}$, where A_0 and A_{bgd} are the initial asymmetry and the background asymmetry, respectively. The experimental data curves shown in Fig. 5a and Supplementary Fig. 4 are described by the model

$$P(t) = P_{KT}(t, \Delta, B) \exp[-(\lambda t)^\beta], \qquad (8)$$

which takes into account both the muon depolarization due to small disordered static internal fields of nuclear origin with a distribution width Δ, as described by the standard Kubo–Toyabe function $P_{KT}(t, \Delta, B)$ (ref. [39]), and the polarization decay due to fluctuating local fields of electronic origin, characterized by the stretched exponential function $\exp[-(\lambda t)^\beta]$. Here λ is the corresponding μSR rate and the stretching exponent $\beta < 1$ denotes a finite distribution of λ. Weak nuclear magnetic fields and experimental background were determined from the field dependence of $A(t)$ at 275 K (Supplementary Fig. 4), which gives $\Delta = 0.062$ mT, $\lambda = 0.007(2)\,\mu s^{-1}$, $\beta = 1$, $A_0 = 0.284$ and $A_{bgd} = 0.055$ (in the dilution-refrigerator set-up the latter parameters are $A_0 = 0.276$ and $A_{bgd} = 0.037$). The muon relaxation at high temperatures and low applied fields is predominantly due to static nuclear fields, as the relaxation due to dynamical fields of electronic origin is weaker. Yet the latter remains the only relaxation mechanism once the applied field exceeds 1 mT (Supplementary Fig. 4). With decreasing temperature, however, the electronic dynamical relaxation mechanism becomes dominant even in zero applied field. The temperature dependence of λ is obtained from fits of equation (8) to the experimental $P(t)$ curves (Fig. 5a) and is shown in Fig. 5b, while the corresponding stretching exponent is shown in Fig. 5d. We note that deviation of β from unity at low temperatures can be related to strong magnetic anisotropy governing the spin dynamics in the ground-state Kramers doublet of $NdTa_7O_{19}$, resulting in a broad distribution of local fields at the muon site. If, alternatively, $\beta < 1$ originated from muons stopping at multiple sites in the unit cell, this parameter would not change with temperature.

Assuming that the dynamics of the local fields are well characterized by a single field-independent electron-spin fluctuation frequency ν_e, λ is inversely proportional to ν_e in the limit of low applied fields ($\gamma_\mu B_0 \ll \nu_e$), as follows from the Redfield relation[39]

$$\lambda = \frac{2\gamma_\mu^2 B_{loc}^2 \nu_e}{\gamma_\mu^2 B_0^2 + \nu_e^2}, \qquad (9)$$

valid in the case of fast fluctuations, that is, for $\nu_e \gg \gamma_\mu B_{loc}$. Here $\gamma_\mu = 135.5 \times 2\pi$ MHz T^{-1} is the muon gyromagnetic ratio and B_{loc} is the width of the distribution of fluctuating local fields. Indeed, the magnetic-field dependence of λ at the lowest temperature of 66 mK follows this dependence (Fig. 5c) and yields the parameters $B_{loc} = 12(1)$ mT and $\nu_e = 120(10)$ MHz, which justify the use of the fast-fluctuation model, as $\gamma_\mu B_{loc} = 10$ MHz.

Combining two independent mechanisms of local-field fluctuations in the fast-fluctuation limit ($\nu_e = \nu_{e,1} + \nu_{e,2}$) then yields $1/\lambda = 1/\lambda_1 + 1/\lambda_2$. Such a model is required to explain the temperature dependence of the μSR rate in $NdTa_7O_{19}$ where we find that the form

$$\frac{1}{\lambda} = \frac{1}{\lambda_0} + \frac{\eta}{\exp\left(\Delta_{\mu SR}/T\right) - 1} \qquad (10)$$

well reproduces the experiment in the whole temperature range (Fig. 5b). Here, the relaxation rate λ_0 is due to spin fluctuations in the CEF ground-state Kramers doublet, while the second term is due to the Orbach process inducing temperature-dependent spin fluctuations with frequency given by equation (6)[39], as found also with ESR, and η characterizes the corresponding μSR rate. Contrary to ESR where these fluctuations of electron spins are probed directly, in μSR the Orbach process does not apply directly to the muon spin but indirectly via magnetic coupling to the electron spins. The fit of the μSR data gives $\lambda_0 = 2.1(1)\,\mu s^{-1}$, $\eta = 52(8)\,\mu s$ and $\Delta_{\mu SR} = 5.7(5)$ meV. We note that single-phonon and Raman-scattering contributions, proportional to T and T^9 (ref. [37]), respectively, are too steep in the relevant temperature ranges, and are thus not relevant in $NdTa_7O_{19}$. The close similarity of $\Delta_{\mu SR} = 5.7(5)$ meV and $\Delta_{ESR} = 6.5(5)$ meV reveals that the CEF splitting is not affected much locally by the implanted muon, which thus likely stops farther away from the Nd^{3+} layers. Moreover, a fully split orbital state of the Kramers ion Nd^{3+} is typically robust to muon-induced distortions, while much stronger effects can occur for non-Kramers ions if the muon lifts the degeneracy of the CEF[59].

Data availability

All data that support the findings of this study are available from the corresponding author upon reasonable request. The inelastic neutron scattering data can be found in ref. [60], the neutron diffraction data in ref. [61], the diffuse neutron scattering data in ref. [62] and the μSR data in ref. [63].

References

51. Zuev, M. G., Politova, E. D. & Stefanovich, S. Y. The X-ray diffraction characteristics and non-linear-optical and electrophysical properties of the tantalates MTa$_7$O$_{19}$ (M= La-Tm, Y). *Russ. J. Inorg. Chem.* **36**, 875–877 (1991).

52. Rodríguez-Carvajal, J. Recent advances in magnetic structure determination by neutron powder diffraction. *Physica B Condens. Matter* **192**, 55–69 (1993).

53. Bain, G. A. & Berry, J. F. Diamagnetic corrections and Pascal's constants. *J. Chem. Educ.* **85**, 532–536 (2008).

54. Stewart, J. R., Andersen, K. H., Cywinski, R. & Murani, A. P. Magnetic diffuse scattering in disordered systems studied by neutron polarization analysis. *J. Appl. Phys.* **87**, 5425–5430 (2000).

55. Paddison, J. A. M., Stewart, J. R. & Goodwin, A. L. Spinvert: a program for refinement of paramagnetic diffuse scattering data. *J. Phys. Condens. Matter* **25**, 454220 (2013).

56. Stevens, K. W. H. Matrix elements and operator equivalents connected with the magnetic properties of rare earth ions. *Proc. Phys. Soc.* **65**, 209 (1952).

57. Arnold, O. et al. Mantid—data analysis and visualization package for neutron scattering and μSR experiments. *Nucl. Instrum. Methods Phys. Res. A* **764**, 156–166 (2014).

58. Newman, D. J. & Ng, B. *Crystal Field Handbook* (Crystal Univ. Press, 2007).

59. Foronda, F. R. et al. Anisotropic local modification of crystal field levels in Pr-based pyrochlores: a muon-induced effect modeled using density functional theory. *Phys. Rev. Lett.* **114**, 017602 (2015).

60. Pregelj, M., Zorko, A., Le, M. D., Arh, T. & Khuntia, P. Crystal-field and magnetic excitations in NdTa$_7$O$_{19}$. STFC ISIS Neutron and Muon Source https://doi.org/10.5286/ISIS.E.RB1920405 (2019).

61. Pregelj, M., Manuel, P., Khuntia, P., Zorko, A. & Arh, T. Quantum spin liquid in the triangular antiferromagnet NdTa$_7$O$_{19}$. STFC ISIS Neutron and Muon Source https://doi.org/10.5286/ISIS.E.RB2000222 (2021).

62. Zorko, A., Arh, T., Mangin-Thro, L. & Pregelj, M. Correlations in the spin-liquid ground state of the Ising triangular antiferromagnet NdTa$_7$O$_{19}$. Institut Laue-Langevin (ILL) https://doi.org/10.5291/ILL-DATA.5-32-930 (2021).

63. Zorko, A., Biswas, P. & Khuntia, P. Spin liquid state in a novel rare-earth based triangular lattice antiferromagnet NdTa$_7$O$_{19}$. STFC ISIS Neutron and Muon Source https://doi.org/10.5286/ISIS.E.RB1910518 (2019).

Author contributions

T.A. and B.S. contributed equally to this work and are both assigned first authorship of the paper. P.K. conceived the investigation of NdTa$_7$O$_{19}$, while A.Z. is the corresponding author who designed this project and supervised the experiments presented in this work. B.S. and P.K. synthesized and structurally characterized the sample. Z.J. and B.S. performed the bulk magnetic measurements. T.A., M.P. and M.D.L. conducted the INS measurements, P.M. conducted the neutron diffraction experiment, and L.M.-T. conducted the diffuse magnetic scattering experiment. M.P. analysed the neutron scattering results and performed the CEF modelling. A.Z. and A.O. performed the ESR measurements, and A.Z. analysed the results. T.A., P.K.B. and A.Z. conducted the μSR investigation; T.A. analysed the corresponding data. All authors discussed the results and the paper. A.Z. wrote the paper, with input provided by M.P. and P.K.

Competing interests

The authors declare no competing interests.

Additional information

Supplementary information The online version contains supplementary material available at https://doi.org/10.1038/s41563-021-01169-y.

Correspondence and requests for materials should be addressed to A. Zorko.

Peer review information *Nature Materials* thanks W. Andrew MacFarlane and the other, anonymous, reviewer(s) for their contribution to the peer review of this work.

Reprints and permissions information is available at www.nature.com/reprints.